Heliyon 10 (2024) e29384

Contents lists available at ScienceDirect

Heliyon

journal homepage: www.cell.com/heliyon

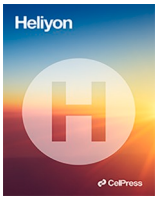

Research article

Phase transformation and strengthening of the gas-atomized $FeCoCrNiMo_{0.5}Al_{1.3}$ high-entropy alloy powder during annealing

Tatiana Larionova [a,*], Anton Semikolenov [a,b], Pavel Kuznetsov [c], Svetlana Shalnova [b], Oleg Tolochko [a,b]

[a] Institute of Machinery, Materials, and Transport, Peter the Great St. Petersburg Polytechnic University, St. Petersburg, 195251, Russia
[b] Institute of Laser and Welding Technologies, State Marine Technical University, St. Petersburg, 190121, Russia
[c] The Federal State Unitary Enterprise "Central Research Institute of Structural Materials "Prometey". Named by I.V. Gorynin of National Research Center "Kurchatov Institute", St. Petersburg, 191015, Russia

ARTICLE INFO

Keywords:
High entropy alloys
Powder
Gas atomization
Annealing
Strengthening
Solid solution decomposition

ABSTRACT

Phase evolution and strengthening of the $FeNiCoCrMo_{0.5}Al_{1.3}$ powder alloy produced via inert gas atomization and annealed in the temperature interval of 300–800 °C have been studied by X-ray diffraction, scanning electron microscopy, energy dispersive X-ray spectroscopy, and microhardness testing. It was found that annealing at 300–600 °C leads to an increase of the element segregations between the several solid solutions with a rise of the lattice misfit *(ε)* to 1.5 % and microhardness growth to 1070 HV. It was assumed that elastic stress caused by the element partitioning is the main strengthening mechanism: microhardness rises linearly with misfit rise with $dHV/d\varepsilon = 43400$ MPa. Sigma arises after the maximum elastic deformation (in 1.5 %) was reached. Formation of the dispersed coherent sigma phase in the annealing interval 600–800 °C results in the microhardness rise. Oxidation that began at 800 °C in 27 h is accompanied with FCC formation due to a depletion of the B2 in Al caused by Al_2O_3 formation. Estimation of the activation energy of the initial stage of the solid solution decomposition gives a very low value in 0.65eV, apparently caused by the high concentration of quenched vacancies. The activation energy of sigma formation approximately coincides with the activation energy of self-diffusion in BCC metals (about 2.60 eV).

1. Introduction

Following the idea being proposed by Cantor [1] and Yeh [2] in 2004, the concept of single-phase alloys being stabilized by high entropy has become widespread among materials scientists over the past two decades. Industrial demand and, to a large extent, scientific curiosity has already led to the development of several new families of multiprincipal alloys or so-called high-entropy alloys (HEA) [3–9]. The first and most studied family of HEAs are alloys based on 3d-transition metals Fe, Ni, Co, Cr, and Mn [3–11]. Based on the general thesis of the concept of HEA, it can be assumed that the reduced Gibbs energy due to high entropy should stabilize a single multicomponent solid solution to its melting point. The absence of precipitation or dissolution is highly desirable for the stability of high-temperature properties, which is important, for example, for the creation of high-temperature alloys or alloys used in additive technologies. However, it has been repeatedly shown that the mechanical properties of single-phase HEAs are rather low, since

* Corresponding author.
E-mail address: larionova_tv@spbstu.ru (T. Larionova).

https://doi.org/10.1016/j.heliyon.2024.e29384
Received 24 November 2023; Received in revised form 19 March 2024; Accepted 7 April 2024
Available online 9 April 2024

solid-solution hardening is much less effective compared to that caused by secondary phase precipitation [3,9,10,12–22]. Along with the solid solution and second-phase hardening the following strengthening effects contributed from elemental diversity have been reported [23]: strain on boundaries of ordered cluster [23,24], strain caused by spinodally modulated structure [16,22,23,25,26], Hall-Petch effect [27]. Recently, eutectic high-entropy alloys composed of FCC and B2 phases have come into the focus of research due to their high fracture strength and tensile ductility. Their main strengthening mechanisms are interface strengthening and stress partitioning effect [27–30]. Refining eutectic cell width and lamellar spacing are accompanied with significant strength growth [31].

In the present work, $FeNiCoCrMo_{0.5}Al_{1.3}$ was chosen for study. According to the Thermo-Calc calculation (Fig. 1), $FeNiCoCrMo_{0.5}Al_{1.3}$ is closed to eutectic composition consisting of sigma and B2 phases. It has a stable phase composition in the interval of 250–1300 °C, with insignificant variation in the amount and composition of the phases until melting.

In the cast condition, the alloy consists of equilibrium B2 (AlNi) and sigma (FeCrMo) phases in almost equal amounts, the alloy microhardness reaches 630 HV [32]. Under rapid melt crystallization via gas atomization only supersaturated BCC solid solution forms [33]. Transformation of the metastable multicomponent solid solution to the equilibrium state can pass via different mechanisms leading to various microstructure formation. Analysis of the binary phase equilibrium diagrams in this system shows different interaction types, such as: ordering (Al–Ni (B2), Fe–Co (B2); Fe–Ni ($L2_1$); spinodal decomposition (Fe–Cr, Mo–Cr); intermetallic phases formation (Fe–Cr, Fe–Mo, Co–Cr, Co–Mo). Since gas atomization has become the most attractive industrial process for large-scale metal powder production intended for the powder bed fusion or spray coating techniques, the ability to adjust the microstructure and properties of the powder as well as control it during consequent consolidation is very important [34–41].

The aim of this work was to study phase and microstructural transformation of the gas-atomized $FeNiCoCrMo_{0.5}Al_{1.3}$ eutectic high-entropy alloy powder during annealing and to investigate their effect on the alloy strengthening. Decomposition of the metastable solid solution in a temperature interval of 300–800 °C was studied using scanning electron microscopy (SEM), energy dispersion spectroscopy (EDS), X-ray diffraction analysis (XRD); and the strengthening was studied by microhardness testing. The relationship of the microstructure evolution and strengthening was emphasized on.

2. Experimental procedure

Initially $FeNiCoCrMo_{0.5}Al_{1.3}$ ingots of mass of approximately 50 g were melted from elemental bulk materials in a high-frequency induction furnace in quartz crucibles under an argon atmosphere. Elemental components with a purity of 99.93 % or greater were used. The melting process took about 2 min, and then the melt was cooled in water. The prepared ingots were 81 used for powder preparation by gas atomization process. The powder of the composition was produced using a HERMIGA 75/3VI atomizer (Phoenix Scientific Industries Ltd, Hailsham, UK). The production parameters are described elsewhere [33]. The produced particles have a spherical shape. A powder size of 20–90 μm was separated for investigation. The chemical composition of the as-atomized powder is presented in Table 1.

Heat treatment of the powder was carried out at temperatures of 300; 400; 500; 600; 700; and 800 °C for 1; 3; 9; and 27 h in an air atmosphere. The phase composition was examined with the D8 Advance diffractometer (BRUKER) using Cu Kα radiation. The lattice parameter was determined on the base of XRD patterns, which had been collected in the 2Θ range from 20° to 140° with a speed of 2°/min. For microscopic observation and microhardness testing the particles were embedded in a resin and polished. SEM and EDS analysis were performed on a MIRA 3 (TESCAN) microscope with AztecLive.Advanced.Ultim.Max.65 EDS (Oxford instruments) detector. Vickers microhardness was tested with a FM-310 (FUTURE-TECH CORP.) under a load of 50 g and a dwelling time of 10 s, at least 7 measurements per point were made. The equilibrium phases were calculated in the Thermo-Calc program using the database "TCHEA 4: High Entropy Alloy v 4.0". The accuracy and calculation speed settings correspond to the standard values.

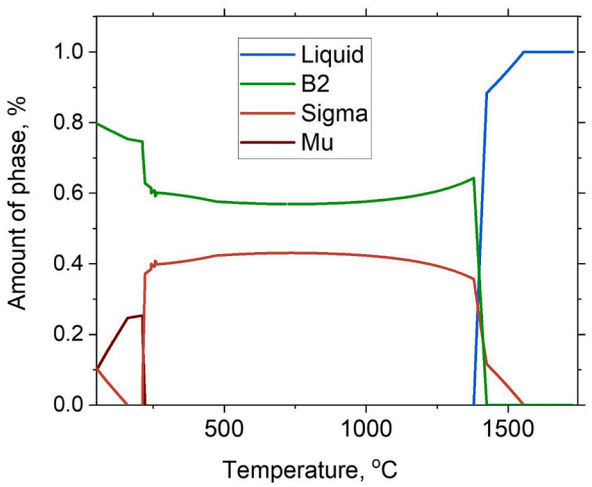

Fig. 1. Equilibrium phases in dependence on the temperature calculated by Thermo-Calc.

Table 1
Chemical composition of the powder.

Atomic concentration, %						
Fe	Ni	Co	Cr	Mo	Al	Si
17.2	17.3	17.2	16.9	9.3	22.0	0.2

3. Results and discussion

3.1. Phase transformation

XRD analysis of the as-atomized powder shows only BCC reflexes, the presence of a weak peak at 30° shows that the BCC solution is partly B2 ordered (Fig. 2,a). It can be noticed that each BCC peak has two sidebands (Inset of Fig. 2,a) denoting the chemical liquation, which is also observed in the microstructure (Fig. 2,b). The observed chemical segregation most likely took place during solidification, which is typical for equiatomic alloys synthesized from elements with large differences in the enthalpy of mixing, such as Al–Ni and Fe–Cr [32]. It is reasonable to assume that XRD reflexes with higher interplanar distances belong to the BCC enriched with elements of larger radius: Mo and Cr.

The microstructures of the particles after annealing for 1 h at different temperatures are presented in Fig. 3. In general, an increase of the annealing temperature leads to an increase of the phase contrast, denoting the growth of the element segregation. After annealing at 800 °C fine homogeneously distributed precipitations are observed in both phases (Fig. 3,j).

XRD patterns of the powders annealed for 1 h and 27 h are shown in Fig. 4a and b. The BCC peaks and their sidebands move with the rise of the annealing temperature or time, reflecting the change in the solid solutions compositions (Fig. 4,c). EDS linear scans of the samples annealed at 400 °C and 600 °C presented in Fig. 5 show two alternating regions enriched in either Mo or Al, each about 2 μm in size; the higher temperature corresponds to the higher concentration gradient between the regions. Elemental compositions of the bright and dark areas are presented in Table 2.

Sigma has been detected after annealing above 600 °C, so the relief on the particles' surface, observed in Fig. 3d and e can be caused namely by the sigma phase formation due to lower specific volume of the sigma compared to that of B2. After the appearance of sigma, BCC sidebands vanished. μ-phase has not been found. Prolonged annealing at 800 °C for 27 h leads to the appearance of pronounced reflections of oxides, especially Al_2O_3, and weak reflections of the FCC solid solution. According to ThermoCalc calculation, B2 and sigma are the only stable phases at temperatures over 230 °C until melting (Fig. 1). However, depletion of the composition in Al leads to the fractional transformation of B2 to FCC solid solution [33].

Fig. 4d and e shows the change of the lattice parameters of the solid solutions in dependence on the annealing temperature. The BCC solid solution enriched with Mo and Cr has the highest lattice parameter, which slightly increases to 2.924 Å as temperature rises. The sidebands corresponding to this solid solution disappear when sigma-phase reflexes appear. The lattice parameter of B2 splits into two values, both of which decrease with the rise of the annealing temperature and at temperatures of 600–700 °C they merge, reaching a value of 2.884 Å close to the equilibrium parameter of AlNi/B2. As seen in the microstructure of the sample annealed for 1 h at 500 °C (Inset of Fig. 3,g), there are layer modulations of the chemical composition within the primary dendrites enriched with Al, the size of each layer does not exceed 50 nm, which may be attributed to the spinodal decomposition of the Al-rich solid solution. Spinodal decomposition in BCC HEA was reported before in AlCoCrFeNi [16], AlCoCrCuFeNi [22], and FeCoNiMnCu [25]. In Ref. [26] spinodal decomposition of high Al-containing composition into random A2 and ordered B2 phases [23] was demonstrated as an effective strengthening mechanism sustaining ductility in high-strength BCC HEA.

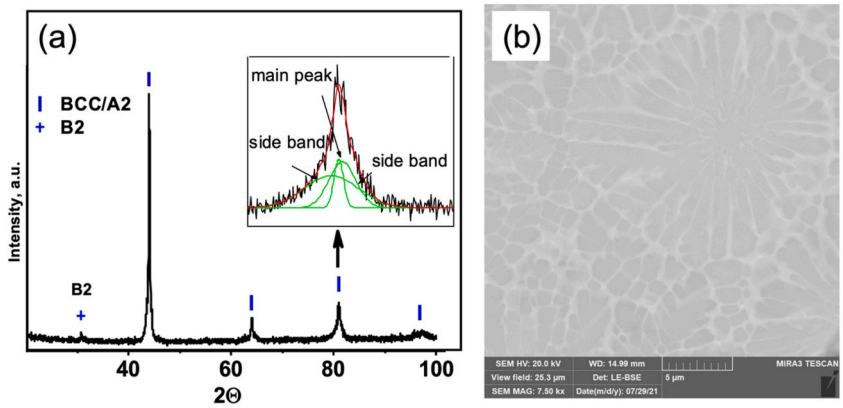

Fig. 2. XRD pattern of the as-atomized powder (a) and microstructure (b).

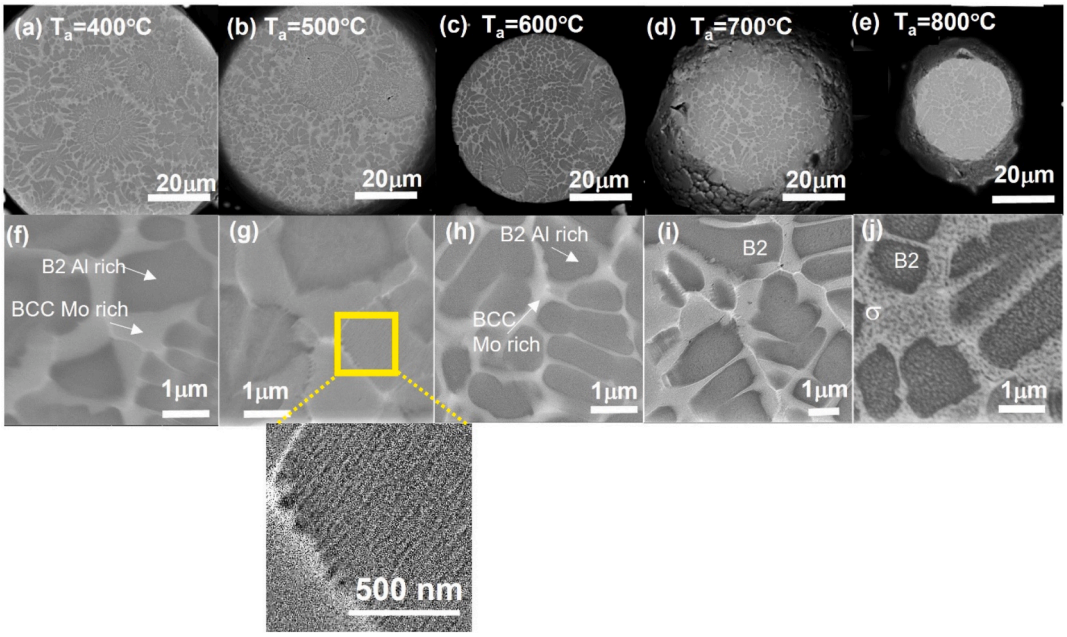

Fig. 3. SEM images of the particles (a–e) and their microstructures (f–j) after annealing for 1 h at 400 °C (a, f); 500 °C (b, g); 600 °C (c, h); 700 °C (d, i); and 800 °C (e, j).

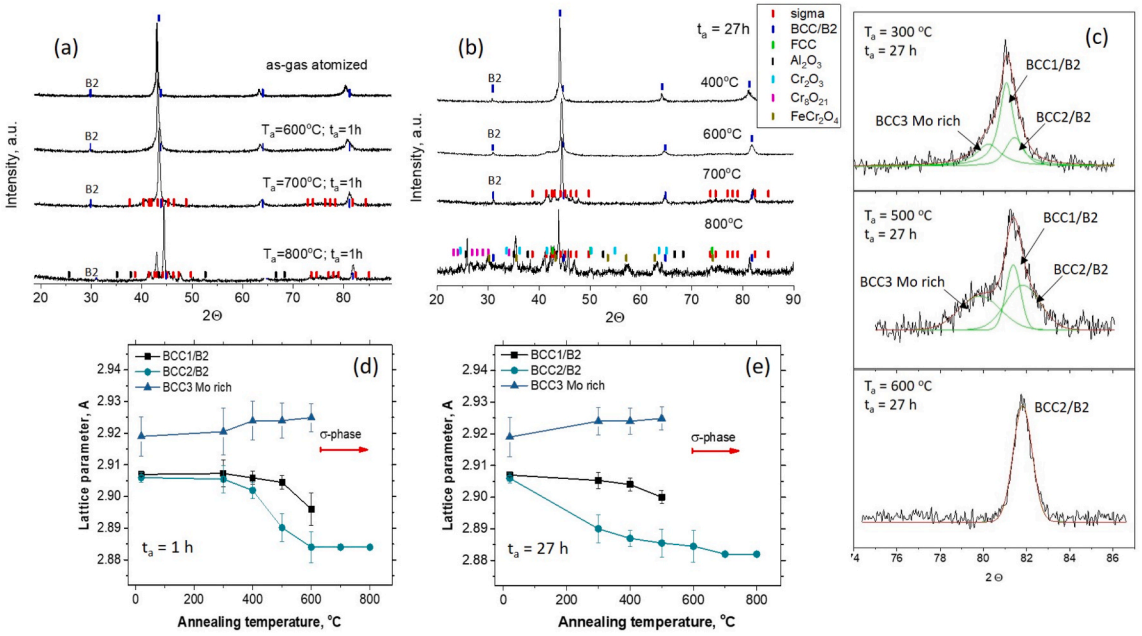

Fig. 4. XRD patterns of the powder in as-atomized condition and after annealing at different temperatures for 1 h (a) and 27 h (b). Magnified XRD peak with sidebands after annealing at different temperatures for 27 h (c). Lattice parameters of the solid solutions formed during annealing at different temperatures for 1 (d) and 27 h (e).

3.2. Strengthening

As it is seen in Fig. 6,a annealing in the interval of 300–600 °C leads to significant strengthening apparently caused by the supersaturated solid solution decomposition. Taking into consideration that in the annealing interval up to 600 °C only segregation between the BCC solid solution is observed, it is assumed that the strengthening effect is caused by the increasing elastic stress contributed from the lattice misfit. Fig. 6,b depicts the change of microhardness as a function of $\varepsilon = (a_1\text{-}a_2)/a_1$, where a_1, a_2 – are

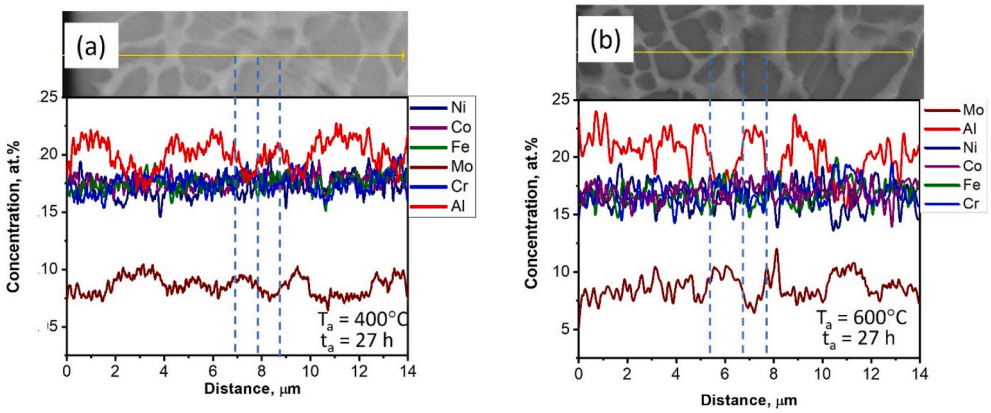

Fig. 5. EDS linear scans for the samples annealed at 400 °C (a) and 600 °C (b) for 27 h.

Table 2
Elemental composition of the bright and dark areas (Fig. 5).

Annealing	Area	Atomic concentration, %					
		Fe	Ni	Co	Cr	Mo	Al
T_a = 400 °C; t_a = 27 h	Bright (Mo-rich)	18.7	16.9	17.5	19.3	9.5	17.5
	Dark (Al-rich)	17.2	18.1	17.6	17.3	7.7	22.0
T_a = 600 °C; t_a = 27 h	Bright (Mo-rich)	19.4	14.9	17.2	19.7	10.8	17.0
	Dark (Al-rich)	15.9	19.0	18.5	16.1	7.3	23.2

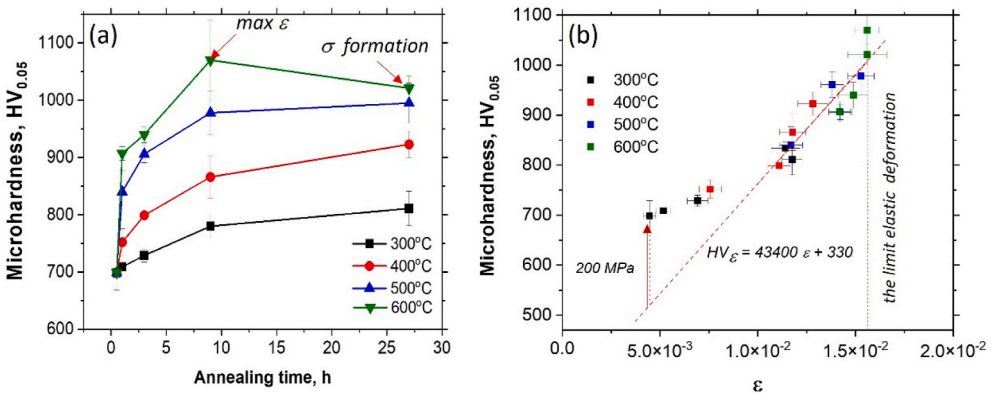

Fig. 6. Change of microhardness in dependence on the annealing time in the annealing interval 300–600 °C (a). Microhardness *vs*. lattice misfit *(ε)*, $\varepsilon = (a_1\text{-}a_2)/a_1$, where a_1, a_2 – are the maximum and minimum lattice parameters (Fig. 4).

maximal and minimal lattice parameters of the solid solutions enriched with Mo and Al correspondingly (Fig. 4e and f). A continuous increase in microhardness is observed with an increase in the lattice misfit (ε) to 1.5 %. As a lattice misfit of 1.5 % is the maximum elastic deformation possible before there is a loss of coherence with the formation of misfit dislocations, and we observed an increase in lattice misfit up to 1.5 % at 600 °C, the temperature at which the sigma phase begins to form, it is likely that the formation of the sigma phase is occurring primarily at the semi coherent boundaries.

Thus, it can be proposed that an elastic stress caused by element partitioning is the main strengthening mechanism in the alloy annealed in the 300–600 °C interval prior to sigma nucleation. The experimental data (at $\varepsilon > 1$ %) are approximated well by linear dependency $HV = 43400\,\varepsilon + 330$. We take attempt to apply the spinodal hardening model to the alloy strengthening at the beginning stage of the solid solution decomposition. Cahn [42] calculated the spinodal hardening due to the coherency internal stresses as a function of amplitude factor *(A)* and wavelength *(λ)* of the composition modulation. In Refs. [32,33] it was proposed that the total magnitude of incremental yield stress in compositionally modulated BCC alloys is determined by two factors: the lattice misfit effect due to the coherent internal stress and the modulus effect due to the spatial variation of elastic modulus:

$$\sigma_{spinodal} = \sigma_\varepsilon + \sigma_G = A\eta E/2(1-\nu) + 0.65\Delta G b/\lambda \quad (1)$$

where, A – amplitude factor of the composition fluctuations ($6A$ – maximal compositional difference [42–44]); $\eta = dlna/dC$ – the relative change of the lattice parameter (a) in dependence of composdition (C); ΔG - the shear modulus variation; b - the Burgers vector; λ – the wavelength of the modulation. Considering the information mentioned above, $A\eta = \varepsilon/6$ and $\sigma_\varepsilon = \varepsilon E/12(1-\nu)$, so the total hardening due to compositional modulation is linear to ε. With $E = 165$ GPa [33] and $\nu \approx 0.3$ and making the assumption that $HV \approx 3\ \sigma$ [45], $dHV_\varepsilon/d\varepsilon \approx 59000$ MPa. The calculated value is close to the experimentally determined slope of the linear dependency: $dHV_\varepsilon/d\varepsilon \approx 43400$ MPa (Fig. 6, b).

An estimation of σ_G taking into account $G = E/2(1+\nu)$; $\Delta E \approx 20$ GPa [33]; $b = 0.25$ nm; and assuming λ as $10 \div 20$ nm, gives value $HV_G \approx 200$ MPa. The wavelength is primarily affected by the aging temperature [42]: the higher temperature results in the higher λ and, correspondingly, lower σ_G, so the modulus variation effect on the hardening should be more pronounced at lower aging temperatures. This fact explains the higher HV values and deviation of the $HV = f(\varepsilon)$ dependency from linear at low aging temperature ($\varepsilon \leq 0.01$).

Change of HV after annealing at 700 °C and 800 °C is shown in Fig. 6. The microhardness increment of the annealed at 700 °C samples is caused by formation of the dispersed coherent sigma phase and correspondingly high area of the interphase boundaries. Annealing at 700 °C for a longer time (27 h) or at 800 °C for 1–3 h leads to a decrease of HV due to coarsening of the sigma and loss of coherency between sigma and BCC/B2. Oxidation that began at 800 °C in 27 h is accompanied with an decrease of microhardness due to depletion of the alloy in Al and Cr.

3.3. Estimation of the activation energy

Activation energy was calculated based on $\ln(t\%) - f(1/T_a)$ plot, where $t\%$ is the time necessary for achievement of preassigned fraction of the solid solution decomposition at each annealing temperature (T_a). Fraction of decomposition was determined according to the change of the main solid solution lattice parameter: 100 % decomposition was assigned to the moment when lattice parameter of the main solid solution (BCC1/B1) reaches value of $a_e = 2.881$ Å, initial state (0 %) corresponds to $a_0 = 2.907$ Å (Fig. 4d and e); a corresponding to 10 % of transformation equals to 2.904 Å $t\%$ was determined on the $a - f(t_a)$ dependency for each annealing temperature as the time when the lattice parameter reaches a required value.

An estimation of the activation energy (E_a) of the initial stage of the solid solution decomposition (calculated for 10 % of transformation) gives a value of about 0.65 eV (Fig. 8,a). This value is much lower than the average activation energy of self-diffusion in any BCC metal and HEA [46]. Such a low activation energy can be the result of a high vacancy concentration due to rapid solidification. Activation energy of vacancy migration in Al (E_m) is equal to 0.65 eV, so it can be assumed that decomposition of the solid solution develops via Al atoms migration by quenched vacancies. We calculate the time of excess vacancy annihilation (τ) according to: $\tau = \alpha R^2/D$, where α — coefficient dependent on the sink geometry; R — distance to the sink, m; D — coefficient of vacancy diffusion, m^2/c; $D = \nu b^2 \exp(-E_m/kT)$. If we assume that the sink is the surface of the particle, then R – the particle radius and $\alpha = 1/\pi^2$. The time of vacancies annihilation calculated using $R_{max} = 90$ μm and $E_m = 0.65$ eV does not exceed 3 min and only several seconds for $T_a = 300$ °C and 500 °C, respectively (Fig. 8,b). Therefore, according to the obtained results excessive vacancies cannot influence the process kinetics. However, quenched vacancies can accelerate diffusion transformations by several orders if the diffusion way is at least two orders less than the distance to the vacancy sink. The wavelength of the composition fluctuation does not exceed 100 nm (Inset of Fig. 3,g) and the distance to the vacancy sink is not less 10 μm (particle's radius). Thus, the assumption about the role of the quenched vacancies in the initial stages of transformation appears reasonable. On the other hand, there are many factors influencing the vacancy mobility, as well as their generation, in multicomponent alloys. Aside from the quenched vacancies, vacancies can appear as a result of the diffusion flows of different elements with very different diffusion coefficients, such as Al and Mo. Higher diffusion mobility of Al compared to that of Mo and Cr leads to diffusion porosity in Mo and Cr enriched area due to the Kirkendall-Frenkel effect (Fig. 7,f).

Such low calculated activation energy (0.65 eV) describes only the beginning of the solid solution decomposition. An estimation of an activation energy for 30 % of transformation as well as sigma formation gives a value of 2.6 eV, which approximately corresponds to the activation energy of self-diffusion determined by the rule of mixture for $FeCoCrNiMo_{0.5}Al_{1.3}$ composition.

The additive manufacture or thermal spraying techniques involves rapid cooling and large temperature gradients, and understanding of the phase evolution in multicomponent metastable/unstable metal compositions during heating is necessary for determination of an processing parameters. The obtained results can be taken into consideration for determination of the effective processing parameters. For example, formation of the sigma phase above 600 °C should lead to the additional internal stresses caused by difference in the specific volumes between matrix and newly formed sigma phase and should be avoided. Above mentioned techniques imply rapid solidification allowing to formation of the supersaturated solution. Post manufacturing heat treatment in the interval of 400–500 °C allow to obtain structure with determined level of internal stress and strengthening.

4. Conclusion

Phase evolution and strengthening of the $FeNiCoCrMo_{0.5}Al_{1.3}$ powder alloy produced via inert gas atomization have been studied by XRD, SEM, EDS methods and microhardness testing.

1) As-atomized particles crystallize in dendrites of partly ordered BCC/B2 supersaturated solid solution with Mo and Cr enriched segregation on the dendrites peripheries.

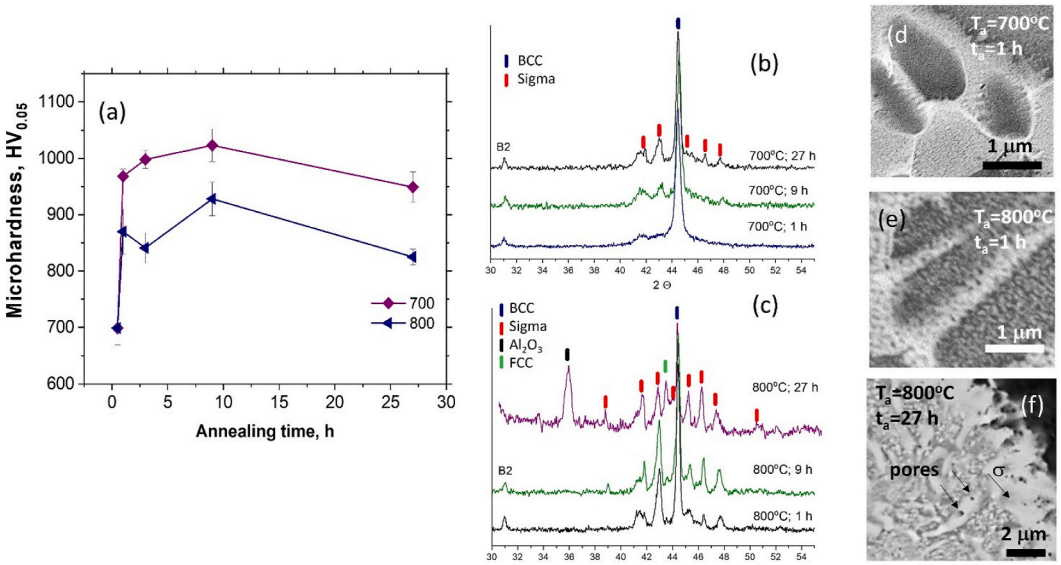

Fig. 7. Change of microhardness in dependence on the annealing time at T_a = 700 °C and 800 °C (a). Results of XRD analysis (b, c) and microstructure (d–f) of the powders annealed at 700 °C (b, d) and 800 °C (c, e, f).

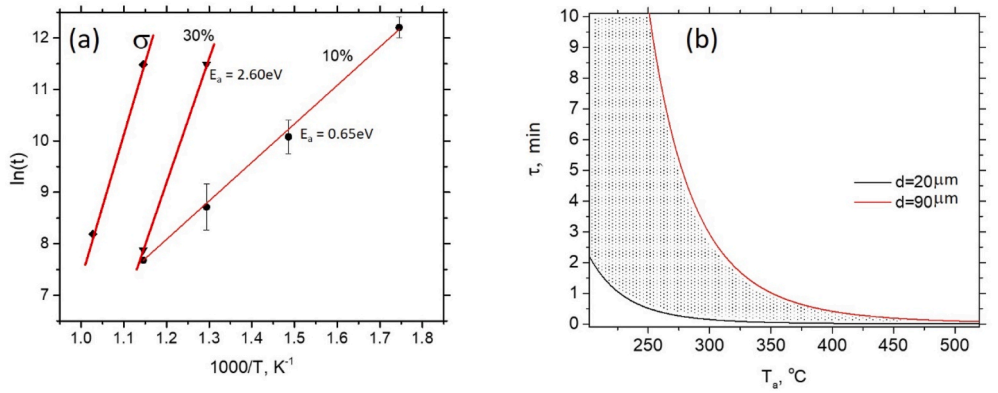

Fig. 8. Activation energy of the 10 %, 30 % solid solution decomposition and sigma appearance (a). Time of the quenched vacancies annihilation in depending on the annealing temperature and particles diameter (b).

2) Annealing in a temperature interval of 300–400 °C leads to an increase of the element segregations and lattice misfit. The lattice misfit increases till $\varepsilon = 1.5$ % accompanied with continuous microhardness growth to 1070 HV. It was assumed that the main strengthening mechanism is elastic stress caused by the element partitioning. The experimental data can be approximated by linear dependency with $dHV/d\varepsilon = 43400$ MPa.
3) Estimation of the activation energy of the initial stage of the solid solution decomposition gives a very low value (0.65 eV), obviously caused by high concentration of quenched vacancies.
4) Sigma arises when the maximum elastic deformation ($\varepsilon = 1.5$ %) is reached, it nucleates at the newly appeared semi-coherent boundaries. Formation of the dispersed coherent sigma phase results in the microhardness rise due to high area of the interphase boundaries. The activation energy of sigma formation approximately coincides with the activation energy of self-diffusion in BCC metals (about 2.6 eV).

Funding

The research is partially funded by the Ministry of Science and Higher Education of the Russian Federation as part of World-class Research Center program (contract No. 075-15-2022-311 dated from April 20, 2022).

Data availability statement

Data included in the article.

CRediT authorship contribution statement

Tatiana Larionova: Writing – review & editing, Writing – original draft, Methodology, Formal analysis, Conceptualization. **Anton Semikolenov:** Validation, Investigation, Formal analysis. **Pavel Kuznetsov:** Resources. **Svetlana Shal'nova:** Investigation. **Oleg Tolochko:** Supervision, Conceptualization.

Declaration of competing interest

The authors declare that they have no known competing financial interests or personal relationships that could have appeared to influence the work reported in this paper.

References

[1] B. Cantor, I.T.H. Chang, P. Knight, A.J.B. Vincent, Microstructural development in equiatomic multicomponent alloys, Mater. Sci. Eng., A 375–377 (2004) 213–218, https://doi.org/10.1016/j.msea.2003.10.257.

[2] J.W. Yeh, S.K. Chen, S.J. Lin, J.Y. Gan, T.S. Chin, T.T. Shun, C.H. Tsau, S.Y. Chang, Nanostructured high-entropy alloys with multiple principal elements: novel alloy design concepts and outcomes, Adv. Eng. Mater. 6 (2004) 299–303, https://doi.org/10.1002/adem.200300567.

[3] D.B. Miracle, O.N. Senkov, A critical review of high entropy alloys and related concepts, Acta Mater. 122 (2017) 448–511, https://doi.org/10.1016/j.actamat.2016.08.081.

[4] W. Steurer, Single-phase high-entropy alloys – a critical update, Mater. Char. 162 (2020) 110179, https://doi.org/10.1016/j.matchar.2020.110179.

[5] X. Yang, Y. Zhang, Prediction of high-entropy stabilized solid-solution in multi-component alloys, Mater. Chem. Phys. 132 (2012) 233–238, https://doi.org/10.1016/j.matchemphys.2011.11.021.

[6] A.S. Rogachev, Structure, stability, and properties of high-entropy alloys, Phys. Met. Metallogr. 121 (2020) 733–764.

[7] P. Sharma, V.K. Dwivedi, ShP. Dwivedi, Development of high entropy alloys: a review, Mater. Today: Proc. 43 (1) (2021) 502–509, https://doi.org/10.1016/j.matpr.2020.12.023, 2021.

[8] E.P. George, D. Raabe, R.O. Ritchie, High-entropy alloys, Nat. Rev. Mater. 4 (2019) 515–534, https://doi.org/10.1038/s41578-019-0121-4.

[9] L. Liu, Y. Zhang, J. Han, X. Wang, W. Jiang, Ch-T. Liu, Zh Zhang, P.K. Liaw, Nanoprecipitate-strengthened high-entropy alloys, Adv. Sci. 8 (2021) 2100870, https://doi.org/10.1002/advs.202100870.

[10] C.W. Huang, P.Y. Su, C.H. Yu, et al., A micromechanical study on the effects of precipitation on the mechanical properties of CoCrFeMnNi high entropy alloys with various annealing temperatures, Sci. Rep. 13 (2023) 3379, https://doi.org/10.1038/s41598-023-30508-z.

[11] N.Yu Yurchenko, N.D. Stepanov, S.V. Zherebtsov, M.A. Tikhonovsky, G.A. Salishchev, Structure and mechanical properties of B2 ordered refractory $AlNbTiVZr_x$ (x = 0–1.5) high-entropy alloys, Mater. Sci. Eng., A 704 (2017) 82–90, https://doi.org/10.1016/j.msea.2017.08.019.

[12] Z. Li, K. Pradeep, Y. Deng, et al., Metastable high-entropy dual-phase alloys overcome the strength–ductility trade-off, Nature 534 (2016) 227–230, https://doi.org/10.1038/nature17981.

[13] L. Guo, D. Xiao, W. Wu, S. Ni, M. Song, Effect of Fe on microstructure, phase evolution and mechanical properties of $(AlCoCrFeNi)_{100-x}Fe_x$ high entropy alloys processed by spark plasma sintering, Intermetallics 103 (2018) 1–11, https://doi.org/10.1016/j.intermet.2018.09.011.

[14] E. Reverte, J. Cornide, M.A. Lagos, M. Campos, P. Alvaredo, Microstructure evolution in a fast and ultrafast sintered non-equiatomic Al/Cu HEA, Metals 11 (2021) 848, https://doi.org/10.3390/met11060848.

[15] C.-J. Tong, Y.-L. Chen, J.-W. Yeh, S.-J. Lin, S.-K. Chen, T.-T. Shun, C.-H. Tsau, S.-Y. Chang, Microstructure characterization of $Al_xCoCrCuFeNi$ high-entropy alloy system with multiprincipal elements, Metall. Mater. Trans. A 36 (2005) 881–893, https://doi.org/10.1007/s11661-005-0283-0.

[16] A. Manzoni, H. Daoud, R. Völkl, U. Glatzel, N. Wanderka, Phase separation in equiatomic AlCoCrFeNi high-entropy alloy, Ultramicroscopy 132 (2013) 212–215, https://doi.org/10.1016/j.ultramic.2012.12.015.

[17] N.D. Stepanov, D.G. Shaysultanov, M.S. Ozerov, S.V. Zherebtsov, G.A. Salishchev, Second phase formation in the CoCrFeNiMn high entropy alloy after recrystallization annealing, Mater. Lett. 185 (2016) 1–4, https://doi.org/10.1016/j.matlet.2016.08.088.

[18] F. Otto, A. Dlouhý, K.G. Pradeep, M. Kuběnová, D. Raabe, G. Eggeler, E.P. George, Decomposition of the single-phase high-entropy alloy CrMnFeCoNi after prolonged anneals at intermediate temperatures, Acta Mater. 112 (2016) 40–52, https://doi.org/10.1016/j.actamat.2016.04.005.

[19] C.C. Juan, C.Y. Hsu, C.W. Tsai, W.R. Wang, T.S. Sheu, J.W. Yeh, S.K. Chen, On microstructure and mechanical performance of $AlCoCrFeMo_{0.5}Ni_x$ high-entropy alloys, Intermetallics 32 (2013) 401–407, https://doi.org/10.1016/j.intermet.2012.09.008.

[20] C. Li, Y. Ma, J. Hao, Y. Yan, Q. Wang, C. Dong, P.K. Liaw, Microstructures and mechanical properties of body-centered-cubic $(Al,Ti)_{0.7}(Ni,Co,Fe,Cr)_5$ high entropy alloys with coherent B2/L21 nanoprecipitation, Mater. Sci. Eng. A. 737 (2018) 286–296, https://doi.org/10.1016/j.msea.2018.09.060.

[21] Y. Ma, B. Jiang, Ch Li, Q. Wang, Ch Dong, P.K. Liaw, F. Xu, L. Sun, The BCC/B2 morphologies in $Al_xNiCoFeCr$ high-entropy alloys, Metals 7 (2017) 57, 110.3390/met7020057.

[22] S. Singh, N. Wanderka, B.S. Murty, U. Glatzel, J. Banhart, Decomposition in multi-component AlCoCrCuFeNi high-entropy alloy, Acta Mater. 59 (1) (2011) 182–190, https://doi.org/10.1016/j.actamat.2010.09.023.

[23] I. Basu, J. ThM. De Hosson, Strengthening mechanisms in high entropy alloys: fundamental issues, Scripta Mater. 187 (2020) 148–156, https://doi.org/10.1016/j.scriptamat.2020.06.019. ISSN 1359-6462.

[24] Q. Zhang, P.K. Liaw, H.J. Yang, J.W. Qiao, Short-range-ordering strengthening and the evolution of dislocation-nucleation modes in an $Fe_{40}Mn_{20}Cr_{20}Ni_{20}$ high-entropy alloy, Mater. Sci. Eng. A. 873 (2023) 145038, https://doi.org/10.1016/j.msea.2023.145038.

[25] Z. Rao, B. Dutta, F. Körmann, W. Lu, X. Zhou, C. Liu, A.K. da Silva, U. Wiedwald, M. Spasova, M. Farle, D. Ponge, B. Gault, J. Neugebauer, D. Raabe, Z. Li, Beyond solid solution high-entropy alloys: tailoring magnetic properties via spinodal decomposition, Adv. Funct. Mater. 31 (2021) 2007668, https://doi.org/10.1002/adfm.202007668.

[26] Z. An, Sh Mao, T. Yang, Ch T. Liu, B. Zhang, E. Ma, H. Zhou, Z. Zhang, L. Wang, X. Han, Spinodal-modulated solid solution delivers a strong and ductile refractory high-entropy alloy, Mater. Horiz. 8 (3) (2021) 948–955, https://doi.org/10.1039/D0MH01341B.

[27] D. Fang, X. Wu, W. Xu, L. Yu, M. Liu, A. Zhang, B. Li, X. Ye, Microstructure and properties of a novel cost-effective FeNi-based eutectic high entropy alloys, Mater. Sci. Eng. A. (2023), https://doi.org/10.1016/j.msea.2023.144919.

[28] Q. Wu, F. He, J. Li, et al., Phase-selective recrystallization makes eutectic high-entropy alloys ultra-ductile, Nat. Commun. 13 (2022) 4697, https://doi.org/10.1038/s41467-022-32444-4.

[29] J. Shen, J.G. Lopes, Zh Zeng, Y.T. Choi, E. Maawad, N. Schell, H.S. Kim, R.S. Mishra, J.P. Oliveira, Deformation behavior and strengthening effects of an eutectic $AlCoCrFeNi_{2.1}$ high entropy alloy probed by in-situ synchrotron X-ray diffraction and post-mortem EBSD, Mater. Sci. Eng.A. 872 (2023) 144946, https://doi.org/10.1016/j.msea.2023.144946.

[30] P. Shi, W. Ren, T. Zheng, et al., Enhanced strength-ductility synergy in ultrafine-grained eutectic high-entropy alloys by inheriting microstructural lamellae, Nat. Commun. 10 (2019) 489, https://doi.org/10.1038/s41467-019-08460-2.
[31] X. Wang, W. Zhai, J.Y. Wang, B. Wei, Strength and ductility enhancement of high-entropy FeCoNi2Al0.9 alloy by ultrasonically refining eutectic structures, Scripta Mater. 225 (2023) 115154, https://doi.org/10.1016/j.scriptamat.2022.115154.
[32] A. Semikolenov, S. Shalnova, V. Klinkov, V. Andreeva, M. Salynova, T. Larionova, O. Tolochko, Effect of Al content on phase compositions of $FeNiCoCrMo_{0.5}Al_x$ high entropy alloy, Metals 11 (2021) 1734, https://doi.org/10.3390/met11111734.
[33] A. Semikolenov, P. Kuznetsov, T. Bobkova, S. Shalnova, O. Klimova-Korsmik, V. Klinkov, I. Kobykhno, T. Larionova, O. Tolochko, Microstructure evolution of $FeNiCoCrAl_{1.3}Mo_{0.5}$ high entropy alloy during powder preparation, laser powder bed fusion, and microplasma spraying, Materials 14 (2021) 7870, https://doi.org/10.3390/ma14247870.
[34] A.O. Moghaddam, N.A. Shaburova, M.N. Samodurova, A. Abdollahzadeh, E.A. Trofimov, Additive manufacturing of high entropy alloys: a practical review, J. Mater. Sci. Technol. 77 (2020) 131–162, https://doi.org/10.1016/j.jmst.2020.11.029.
[35] Z.U. Arif, M.Y. Khalid, A.A. Rashid, E. Rehman, A. Muhammad, Laser deposition of high-entropy alloys: a comprehensive review, Opt. Laser Technol. 145 (2022) 107447, https://doi.org/10.1016/j.optlastec.2021.107447.
[36] P. Patel, S.A. Alidokht, N. Sharifi, et al., Microstructural and tribological behavior of thermal spray CrMnFeCoNi high entropy alloy coatings, J. Therm. Spray Technol. 31 (2022) 1285–1301, https://doi.org/10.1007/s11666-022-01350-y.
[37] B. Karlsson, P. Beran, L. Riekehr, J.-Ch Tseng, P. Harlin, U. Jansson, J. Cedervall, Structure and phase transformations in gas atomized AlCoCrFeNi high entropy alloy powders, J. Alloys Compd. 893 (2022) 162060, https://doi.org/10.1016/j.jallcom.2021.162060.
[38] J. Lehtonen, Y. Ge, N. Ciftci, O. Heczko, V. Uhlenwinkel, S.-P. Hannula, Phase structures of gas atomized equiatomic CrFeNiMn high entropy alloy powder, J. Alloys Compd. 827 (2020) 154142, https://doi.org/10.1016/j.jallcom.2020.154142.
[39] A. Anupam, R.S. Kottada, S. Kashyap, A. Meghwal, B.S. Murty, C.C. Berndt, A.S.M. Ang, Understanding the microstructural evolution of high entropy alloy coatings manufactured by atmospheric plasma spray processing, Appl. Surf. Sci. 505 (2020) 144117, https://doi.org/10.1016/j.apsusc.2019.144117.
[40] J.-T. Liang, K.-Ch Cheng, Sh-H. Chen, J.-H. Chen, S. Stadler, Ch-L. Li, Ch-H. Hsueh, Study on the continuous phase evolution and physical properties of gas-atomized high-entropy alloy powders, Mater. Res. Express 7 (2) (2020) 7, https://doi.org/10.1088/2053-1591/ab5ee2.
[41] J. Ren, Y. Zhang, D. Zhao, et al., Strong yet ductile nanolamellar high-entropy alloys by additive manufacturing, Nature 608 (2022) 62–68, https://doi.org/10.1038/s41586-022-04914-8.
[42] J.W. Gahn, Hardening by spinodal decomposition, Acta Metall. 11 (Issue 12) (1963) 1275–1282, https://doi.org/10.1016/0001-6160(63)90022-1.
[43] M. Kato, Hardening by spinodally modulated structure in b.c.c. alloys, Acta Metall. 29 (1) (1981) 79–87, https://doi.org/10.1016/0001-6160(81)90088-2.
[44] M. Kato, T. Mori, L.H. Schwartz, Hardening by spinodal modulated structure, Acta Metall. 28 (3) (1980) 285–290, https://doi.org/10.1016/0001-6160(80)90163-7.
[45] X. Fan, R. Qu, Z. Zhang, Relation between strength and hardness of high-entropy alloys, Acta Metall. Sin. 34 (2021) 1461–1482.
[46] J. Dąbrowa, M. Danielewski, State-of-the-Art diffusion studies in the high entropy alloys, Metals 10 (2020) 347, https://doi.org/10.3390/met10030347.